Deutsches Elektronen-Synchrotron DESY

Machine learning-assisted measurement of azimuthal angular asymmetries in deep-inelastic scattering with the H1 detector

H1 Collaboration

Abstract

Jet-lepton azimuthal asymmetry harmonics are measured in deep inelastic scattering data collected by the H1 detector using HERA Run II collisions. When the average transverse momentum of the lepton-jet system, $|\vec{P}_\perp|$, is much larger than the total transverse momentum of the system, $|\vec{q}_\perp|$, the asymmetry between $\vec{P}_\perp$ and $\vec{q}_\perp$ is expected to be generated by initial and final state soft gluon radiation and can be predicted using perturbation theory. Quantifying the angular properties of the asymmetry therefore provides a novel test of the strong force and is also an important background to constrain for future measurements of intrinsic asymmetries generated by the proton's constituents through Transverse Momentum Dependent (TMD) Parton Distribution Functions (PDF). Moments of the azimuthal asymmetries are measured using a machine learning technique that does not require binning and thus does not introduce discretization artifacts.

1 Introduction

Due to momentum conservation, the outgoing objects in collision systems, such as hadronic jets or leptons, are nearly back-to-back in the transverse plane. Large deviations from this back-to-back configuration can be generated in reactions producing more than two outgoing objects or when one of the outgoing objects undergoes a hard, wide-angle emission. Small deviations can also be generated by initial and final state radiation, also from the intrinsic structure of the colliding particles when at least one is a hadron. Sources of these deviations include the elliptic gluon Wigner distributions [1–6], intrinsic momentum of polarized gluons within the hadron [7–13] that are predicted to generate a $\cos(2\phi)$ asymmetry. More recently, this observable is predicted to be sensitive saturation phenomena [14]. The goal of this measurement is to probe a region of phase space where extrinsic contributions to the asymmetry are expected to dominate [15] that have nothing to do with the non-trivial intrinsic structure of the target hadron. This may provide essential constraints for future explorations of intrinsic asymmetries.

The data used in this study are from deep inelastic scattering (DIS) events collected by the H1 detector using positron-proton collisions from the HERA II collider. Events with a high squared momentum transfer between the lepton and proton, Q^2, are examined in the laboratory frame for the imbalance between the scattered electron and outgoing jet. Previous measurements of lepton-jet correlations in the laboratory frame using the same dataset explored various kinematic properties [16, 17]. The measurement in Ref. [16] was performed simultaneously in the lepton kinematic properties, the jet transverse[1] momentum, the jet pseudorapdiity η, the relative transverse electron-jet momentum imbalance q_T/Q, and the angular separation in the transverse plane, $\Delta\phi$. The results were presented as four binned differential cross section measurements. Reference [17] extended this result by presenting the four observables in bins of Q^2 and inelasticity. The goal of the current analysis is to extend the previous results by measuring the moments of the azimuthal asymmetry harmonics as a function of total transverse momentum, $q_\perp$.

The previous simultaneous eight-dimensional measurement was enabled by the machine learning-based unfolding method MULTIFOLD [18, 19]. In addition to the lepton-jet studies described above, MULTI-FOLD has also been used to measure properties of jet substructure [20, 21]. A key feature of MULTIFOLD is that it is unbinned, so the measurement of moments is unaffected by binning artifacts. As the goal of the present analysis is to measure moments as a function of energy scale, the unbinned nature of MULTIFOLD will play a critical role in achieving a precise result.

This note is organized as follows. Section 2 introduces the H1 detector and the analysis observables. Then, Sec. 3 describes the Monte Carlo simulated datasets used for the analysis. Corrections for detector effects (unfolding) using the MULTIFOLD algorithm are detailed in Sec. 4. Uncertainty estimation is detailed in Sec. 5. Theoretical predictions using Quantum Chromodynamics (QCD) and experimental results are presented in Sec. 6 and the note ends with conclusions and outlook in Sec. 7.

2 Experimental method

A full description of the H1 detector can be found elsewhere [22–26] while the detector components that are most relevant for this measurement are described below. The main sub-detectors used in this analysis are the inner tracking detectors and the Liquid Argon (LAr) calorimeter, which are both immersed in a magnetic field of 1.16 T provided by a superconducting solenoid. The central tracking system, which covers $15° < \theta < 165°$ and the full azimuthal angle, consists of drift and proportional chambers that are complemented with a silicon vertex detector in the range $30° < \theta < 150°$ [27]. It yields a transverse momentum resolution for charged particles of $\sigma_{p_T}/p_T = 0.2\% \, p_T/\text{GeV} \oplus 1.5\%$. The LAr calorimeter, which covers $4° < \theta < 154°$ and full azimuthal angle, consists of an electromagnetic section made of

---

[1]This measurement uses a right handed coordinate system defined such that the positive z direction points in the direction of the proton beam and the nominal interaction point is located at $z = 0$. The polar angle θ, is defined with respect to this axis. The pseudorapidity is defined as $\eta_{\text{lab}} = -\ln\tan(\theta/2)$. For this work, we are using $\eta = \eta_{\text{lab}}$.

lead absorbers and a hadronic section with steel absorbers; both are highly segmented in the transverse and longitudinal directions. Its energy resolution is $\sigma_E/E = 11\%/\sqrt{E/\text{GeV}} \oplus 1\%$ for leptons [28] and $\sigma_E/E \approx 50\%/\sqrt{E/\text{GeV}} \oplus 3\%$ for charged pions [29]. In the backward region ($153° < \theta < 177.5°$), energies are measured with a lead-scintillating fiber calorimeter [26]. Results are reported using the data recorded by the H1 detector in the years 2006 and 2007 when positrons and protons were collided at energies of 27.6 GeV and 920 GeV, respectively. The total integrated luminosity of this data sample corresponds to 228 pb^{-1} [30].

Events are triggered by requiring a high energy cluster in the electromagnetic part of the LAr calorimeter. The scattered lepton is identified as the highest transverse momentum LAr cluster matched to a track passing an isolation criteria [31]. Events containing scattered leptons with energy $E_{e'} > 11$ GeV are kept for further analysis, resulting in a trigger efficiency higher than 99.5% [32, 33]. Backgrounds from additional processes such as cosmic rays, beam-gas interactions, photoproduction, charged-current DIS and Quantum Electrodynamics (QED) Compton processes are rejected after dedicated selection [33, 34], resulting in negligible background contamination.

This work aims to measure the azimuthal angular asymmetry between the scattered lepton and reconstructed jet - see Fig. 1. This asymmetry is denoted as ϕ, and is calculated as the azimuthal angle between total lepton-jet transverse momentum,

$$\vec{q}_\perp = \vec{k_{l\perp}} + \vec{k_{\text{J}\perp}}, \tag{1}$$

and the average lepton-jet transverse momentum,

$$\vec{P}_\perp = (\vec{k_{l\perp}} - \vec{k_{\text{J}\perp}})/2. \tag{2}$$

Thus, ϕ is given by:

$$\phi = \cos^{-1}[(\vec{q}_\perp \cdot \vec{P}_\perp)/(|\vec{q}_\perp| \cdot |\vec{P}_\perp|)]. \tag{3}$$
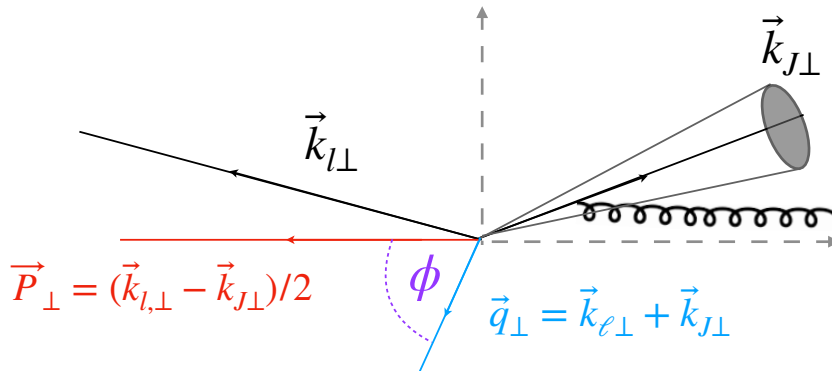
Fig. 1: Lepton-jet final state in the transverse plane perpendicular to the beam direction. The lepton-jet total transverse momentum is labeled $\vec{q}_\perp = \vec{k_{l\perp}} + \vec{k_{\text{J}\perp}}$. The average lepton-jet transverse momentum is denoted $\vec{P}_\perp = (\vec{k_{l\perp}} + \vec{k_{\text{J}\perp}})/2$. The angle between the two vectors is designated ϕ. While the soft gluon (sg) radiation tends to be collinear to the jet axis, radiation that falls outside of the jet radius can result in a measurable lepton-jet momentum asymmetry. For this simple schematic, $\vec{q}_\perp = -\vec{k}_{sg\perp}$ from momentum conservation.

The measurement is presented in terms of three harmonics of ϕ: $\cos(\phi), \cos(2\phi)$, and $\cos(3\phi)$, as relevant perturbative QCD calculations obtain the azimuthal angle anisotropies of two-particle (or jet) correlations through harmonic analysis that extracts the Fourier coefficients for $\cos(\phi), \cos(2\phi)$, and $\cos(3\phi)$.

For events where $P_\perp \gg q_\perp$, soft gluon radiation can dominate the asymmetry. This is because radiative corrections are thought to be enhanced by large double logarithms: $\alpha \ln^2(P_\perp^2/q_\perp^2)^n$ [15]. To facilitate comparisons to perturbative QCD (pQCD) calculations and to satisfy the condition $P_\perp \gg q_\perp$, only events with $q_\perp/p_T^{jet} \leq 0.3$ are selected. Note that $P_\perp \approx p_T^{jet}$ after our kinematic selection.

DIS reactions are governed by the momentum transferred between the lepton and proton squared, Q^2, and the inelasticity y, or equivalently, the longitudinal momentum fraction $x = Q^2/(sy)$. The Σ method [35] is used to reconstruct Q^2 and y as:

$$Q^2 = \frac{E_{e'}^2 \sin^2 \theta_{e'}}{1-y} \tag{4}$$

$$y = \frac{\sum_{i \in \text{had}}(E_i - p_{i,z})}{\sum_{i \in \text{had}}(E_i - p_{i,z}) + E_{e'}(1 - \cos\theta_{e'})}, \tag{5}$$

where $\theta_{e'}$ is the polar angle of the scattered lepton and $\sum(E_i - p_{i,z})$ is the total difference between the energy and longitudinal momentum of the entire hadronic final state. Compared to other methods, the Σ reconstruction reduces sensitivity to collinear initial state QED radiation, $e \to e\gamma$, since the beam energies are not included in the calculation.

The FASTJET 3.3.2 package [36, 37] is used to cluster jets in the laboratory frame with the inclusive k_T algorithm [38, 39] and distance parameter $R = 1$. The inputs for the jet clustering are hadronic final state (HFS) objects with $-1.5 < \eta < 2.75$. These objects are built from calorimeter-cell clusters and reconstructed tracks, after removing those associated with the scattered lepton, using an energy flow algorithm [40–42]. Jets with transverse momentum $p_T^{jet} > 5$ GeV are selected for further analysis.

The input for the jet clustering at the generator level ("particle level") are final-state particles with proper lifetime $c\tau > 10$ mm, excluding the scattered lepton. Reconstructed jets (reco) are matched to the generated jets (gen) with an angular distance selection of $\Delta R^2 = (\phi_{\text{gen}}^{jet} - \phi_{\text{reco}}^{jet})^2 + (\eta_{\text{gen}}^{jet} - \eta_{\text{reco}}^{jet})^2 < 0.9^2$.

Events with $Q^2 > 150$ GeV^2, $0.08 < y < 0.7$, and at least one jet participate in the unfolding (Sec. 4). The final measurement is presented using the leading jet in the event within a fiducial volume defined by $Q^2 > 150$ GeV^2, $0.2 < y < 0.7$, $p_T^{jet} > 10$ GeV, $-1.0 < \eta^{jet} < 2.5$, and $q_\perp/p_T^{jet} \leq 0.3$.

3 Monte Carlo simulations

Monte Carlo (MC) simulations are used to correct the data for detector acceptance and resolution effects as well as to compare theoretical predictions with unfolded results.

Detector acceptance and resolution effects are estimated using DJANGOH [43] 1.4 and RAPGAP [44] 3.1 simulators. Both generators implement Born level matrix elements for neutral current DIS, boson–gluon fusion, and QCD Compton processes and are interfaced with HERACLES [45–47] for QED radiation. The CTEQ6L PDF set [48] and the Lund hadronization model [49] with parameters determined by the ALEPH Collaboration [50] are used for the non-perturbative components. DJANGOH uses the Colour Dipole Model as implemented in ARIADNE [51] for higher order emissions, and RAPGAP uses parton showers in the leading logarithmic approximation. Each of these generators is combined with a detailed simulation of the H1 detector response based on the GEANT3 simulation program [52] and reconstructed in the same way as data.

Predictions from PYTHIA 8.3 [53, 54] are used for comparison using the default implementation and two additional parton shower implementations: VINCIA [55, 56] and DIRE [57]. VINCIA uses a p_T-ordered model for QCD + QED showers based on the antenna formalism while DIRE implements a p_T ordered dipole shower similar to ARIADNE. The NNPDF3.1 PDF set [58] is used for both default and VINCIA implementation and MMHT14nlo68cl PDF set [59] is used for the DIRE implementation.

Predictions from HERWIG 7.2 [60, 61] are calculated using the default implementation parameters and the CT14 [62] PDF set.

4   Unfolding

The unfolding procedure for this measurement, MULTIFOLD, is the same one used in [63]. A key advantage of MULTIFOLD is the re-usability of the unfolded events, as demonstrated with this measurement. The MULTIFOLD method is an iterative two-step (expectation-maximization) procedure to correct for detector effects. The goal is to infer particle-level data using detector-level data and simulations. The main components of MULTIFOLD are explained in more detail below.

The unfolded phase space will consist of $\vec{x} = (p_x^e, p_y^e, p_z^e, p_T^{\text{jet}}, \eta^{\text{jet}}, \phi^{\text{jet}}, q_\perp/Q, \Delta\phi^{\text{jet}})$. p_x^e, p_y^e, and p_z^e are the $\hat{x}, \hat{y}$, and $\hat{z}$ component of the lepton momentum in cartesian coordinates, respectively. p_T^{jet} and η^{jet} are the transverse momentum and pseudorapidity of the jet. ϕ^{jet} is the azimuthal angle of the jet, measured in the transverse plane in the lab system, not to be confused with the primary observable of this work, ϕ, which is taken as the angle between $\vec{P}_\perp$ and $\vec{q}_\perp$. $q_\perp/Q$ is the total transverse momentum of the event devidide by the momentum transfer square. Lastly, $\Delta\phi^{\text{jet}}$ is the azimuthal angle measured between the jet and the lepton in the transverse plane.

The first step of MULTIFOLD uses observables at detector level while the second step operates at particle level. Let $X_{\text{data}} = \{\vec{x}_i\}$ be the set of events in data and $X_{\text{MC,gen}} = \{\vec{x}_{\text{gen},i}\}$ and $X_{\text{MC,reco}} = \{\vec{x}_{\text{reco},i}\}$ be sets of events in simulation with a correspondance between the two sets. In simulation, there are a set of observables at particle-level and detector-level for each event. If an event does not pass the particle-level or detector-level event selection, then the corresponding set of observables are assigned a dummy value $\vec{x} = \emptyset$. Each event i in simulation is also associated with a weight w_i from the MC simulation.

MULTIFOLD achieves an unbinned unfolding by iteratively reweighting the particle-level events. Each event i in simulation is given a weight ν_i and these weights are updated at each iteration. The final result is the simulated events with weights $\nu_i w_i$. From these events, one can compute new observables defined on $\vec{x}$ and can construct histograms or other summary statistics. The MULTIFOLD weights are initialized at $\nu_i = 1$, i.e. the prior is the initial MC simulation.

The first step of MULTIFOLD is to train a classifier f to distinguish the weighted simulation at detector-level from the data. The classifier is trained to maximize the common binary cross entropy:

$$\sum_{\vec{x}_i \in X_{\text{data}}} \log(f(\vec{x}_i)) + \sum_{\vec{x}_i \in X_{\text{MC,reco}}} \nu_i w_i \log(1 - f(\vec{x}_i)), \tag{6}$$

where both sums only include events that pass the detector-level selection. For events that pass the detector-level selection, define $\lambda_i = \nu_i \times f(\vec{x}_i)/(1 - f(\vec{x}_i))$ for $\vec{x}_i \in X_{\text{MC,reco}}$. This manipulation of the classifier output is known (see e.g. Refs. [64, 65]) to produce an estimate of the likelihood ratio between data and simulation. For events that do not pass the detector-level selection, $\lambda_i = \nu_i$.

The second step of MULTIFOLD is a regularization step. The weights λ_i are insufficient because they are not a proper function of the particle-level phase space. In other words, a single phase space point $\vec{x}_{\text{gen}}$ can be mapped to different $\vec{x}_{\text{reco}}$ values under the stochastic detector response. The second step of MULTIFOLD averages the weights λ for a fixed particle-level phase space point. This is accomplished by training a classifier to distinguish the particle-level simulation weighted by ν from the particle-level simulation weighted by λ. The loss function is once again the binary cross entropy:

$$\sum_{\vec{x}_i \in X_{\text{MC,truth}}} \lambda_i w_i \log(f(\vec{x}_i)) + \nu_i w_i \log(1 - f(\vec{x}_i)), \tag{7}$$

where the sum only includes events that pass the particle-level selection. For events that pass the particle-level selection, define $v_i = v_i \times f(\vec{x}_i)/(1 - f(\vec{x}_i))$ for $\vec{x}_i \in X_{\text{MC,truth}}$. For events that do not pass the particle-level selection, v_i is left unchanged from its previous value.

The classifiers for Steps 1 and 2 are parameterized as fully connected deep neural networks. These networks are implemented in TENSORFLOW [66] and KERAS [67] and optimized using ADAM [68]. The input layer to the neural networks has 8 nodes, corresponding to the 8 dimensions of $\vec{x}$ used for unfolding. All inputs are standardized so that each dimension of $\vec{x}$ has mean zero and unit standard deviation. Following the input, there are three hidden layers, with 50, 100, and 50 nodes, respectively. Each layer has a rectified linear unit activation function and the network output is a single node with the sigmoid activation function. None of these hyperparameters were optimized and all other hyperparemeters are set to their default values. In particular, the network biases are all initialized to zero and the weights are initilaized using the Glorot uniform distribution [69]. In order to minimize variations from the stochastic nature of the training procedure, 10 networks are trained for each configuration and the final result is taken as the median over the 10 values per event.

For training, the inputs are partitioned equally into a training and validation set. This partition is random and redone at each iteration. Training proceeds for 10,000 epochs with an early stopping mechanism that halts training if the validation loss does not decrease for 10 consecutive epochs. Step 1 training uses a batch size of 50,000 events and a learning rate of 2×10^{-6}, while step 2 training uses a batch size of 100,000 events and a learning rate of 5×10^{-6}. The networks are trained using NVIDIA Quadro RTM 6000 Graphical Processing Units (GPUs). These GPUs have sufficient memory (24 GB) to simultaneously fit all of the inputs and the model into memory. The training time for both Step 1 and Step 2 decreases with each iteration since the MC at particle level is reweighted to successively better match the data with each iteration. For instance, the first iteration of Step 1 takes 3350 seconds and Step requires 2500 seconds. In the fifth iteration, Step 1 only takes 660 seconds and Step 2 requires 540 seconds.

5 Uncertainties

Systematic uncertainties on the description of the detector are estimated by varying the relevant aspects of the simulation and carrying out the full unfolding procedure with the varied simulation set.

As the main observable of this work ϕ, is calculated from the outgoing 4-momenta of the scattered lepton and hadronic final state, their uncertainties (in particular energy scale and azimuthal angle) are carefully considered. Uncertainties on HFS energy scale are attributed to two different contributions: HFS objects contained in high $p_T t$ jets and other remaining HFS objects. The energy-scale uncertainty in both cases is $\pm 1\%$. Both sources of uncertainty are estimated separately [70, 71] by varying the each HFS energy by $\pm 1\%$. An uncertainty of ± 20 mrad is assigned to the azimuthal angle determination of HFS objects. The uncertainties on the lepton energy scale ranges from $\pm 0.5\%$ to $\pm 1\%$ [71, 72]. Uncertainties on the azimuthal angle of the scattered lepton are estimated to be ± 1 mrad [73].

Additional uncertainties from the unfolding procedure are estimated to cover a possible bias from the generator choice used to perform the unfolding procedure. Those include a model bias, estimated by the difference in results obtained when performing the unfolding with the RAPGAP or DJANGOH simulations. For the $\cos(2\phi)$ and $\cos(3\phi)$ harmonics, the model uncertainty is the leading uncertainty. The model bias is plotted together with the nominal results in Figure 2.

QED corrections accounting for virtual and real higher-order QED effects are taken as an uncertainty and are estimated by comparing the simulation response with and without initial QED radiation with residual differences taken as the uncertainty. The mean azimuthal angular asymmetry of the events that pass our selection is reported, thus normalization uncertainties, such as luminosity scale and trigger efficiencies are not considered.
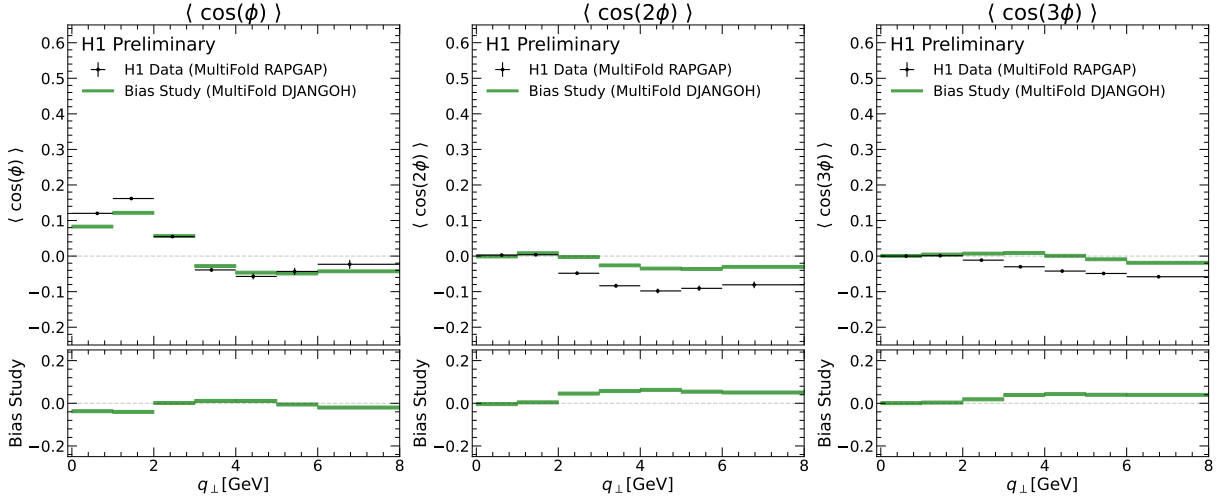
Fig. 2: The nominal results (black points) plotted with the model bias (green bars) for the three harmonics of the azimuthal angular asymmetry, $\cos(\phi), \cos(2\phi)$, and $\cos(3\phi)$ plotted as a function of $q_\perp$. The bottom panel shows the absolute difference between the bias study and the nominal results. The model bias represents the leading uncertainty for the $\cos(2\phi)$ and $\cos(3\phi)$ harmonics.

The statistical uncertainty is estimated using the bootstrap technique [74]. The unfolding procedure is repeated on 100 pseudo datasets, each defined by resampling the original dataset according to a Poisson distribution with $\mu = 1$. The number of MC events exceeds the number of data events by nearly two orders of magnitude and therefore the MC statistical uncertainty is negligible compared to the corresponding data uncertainty. Due to the ensembling procedure described in Sec. 4, variations from the random nature of the network initialization and training are negligible compared to the data statistical uncertainty.

The major sources of uncertainty are plotted in Fig 2 as a function this measurement's independent variable, $q_\perp$. The uncertainties are reported as absolute quantities due to the central values of the measurement being very close to 0.

6   Results

Unfolded results are presented as a function of $q_\perp$. The $\cos(\phi)$, $\cos(2\phi)$, and $\cos(3\phi)$ harmonics of the lepton-jet azimuthal angular asymmetry are shown in Figure 3 and are compared to various Monte Carlo generators (PYTHIA, RAPGAP, and DJANGO).

The measurements are also compared to a perturbative QCD calculation involving soft-collinear gluon resummation for similar kinematics [15]. While there is reasonable agreement within uncertainties for the $\cos 2\phi$ and $\cos 3\phi$ distributions, the first harmonics shows a sizable disagreement with measured data. The pQCD calculation does accurately predict, however, that the $\cos(\phi)$ term to be the leading term is the lepton-jet events. Nonetheless, the disagreement in the $\cos(\phi)$ distributions could indicate non-perturbative contributions (or more relevantly, suppression) of the asymmetry. Additional studies requiring larger p_T^{jet} may provide insight into the magnitude of non-perturbative contributions.

This observable was also calculated with kinematics relevant for the upcoming electron ion collider experiment [14]. While the observable is the same, the physical source of the asymmetry was calculated for gluon saturation effects. Conclusions from the comparison of these models to this specific measurement should be drawn cautiously, as the calculations were performed with different kinematics as input[2]. Two

---

[2]We are reaching out to the authors to see if they can recalculate the results for our kinematics, and more importantly with a jet resolution parameter of 1.0, instead of the 0.4 in the paper. For now I'm excluding the gluon saturation calculations

of the calculations performed express the quark distribution in terms of a dipole scattering amplitude. They then use a solution to the Sudakov suppressed Balitsky-Kovchegov (rcBK solution) [75] evolution equation as input dipole scattering amplitude for one calculation, and a 3-parameter model fit to HERA data labelled as Golec-Biernat and Wusthoff (GBW) model, that aims to describe saturation phenomena at low Q^2 [76]. The final and third calculation uses the CT18A PDF that involves a next-to-leading order (NLO) TMD calculation using collinear PDFs [77]. Importantly, all three calculations require small $q_\perp$, $q_\perp < 3.0$ GeV. All three calculations deviate from measured data substantially for $\cos(\phi)$ and $\cos(2\phi)$ distributions, but agree within uncertainties for $\cos(3\phi)$. This may indicate an over estimate of contributions from gluon saturation, but more precise comparisons with matching kinematics would be required for future studies.

Three PYTHIA models are compared to the data with varying agreement for each harmonic. PYTHIA + VINCIA shows the best agreement with the measured data for $\cos(\phi)$, however shows the largest deviation from data for $\cos(2\phi)$. PYTHIA and PYTHIA + DIRE are very similar for the most part, and show good agreement with the measured data for all $q_\perp$ bins for $\cos(2\phi)$, but deviated from the data at low $q_\perp$ for $\cos(\phi)$. All three PYTHIA predictions for $\cos(3\phi)$ agree with data within uncertainties. RAPGAP and DJANGO agree with the measured data for almost all $q_\perp$ bins for all harmonics.
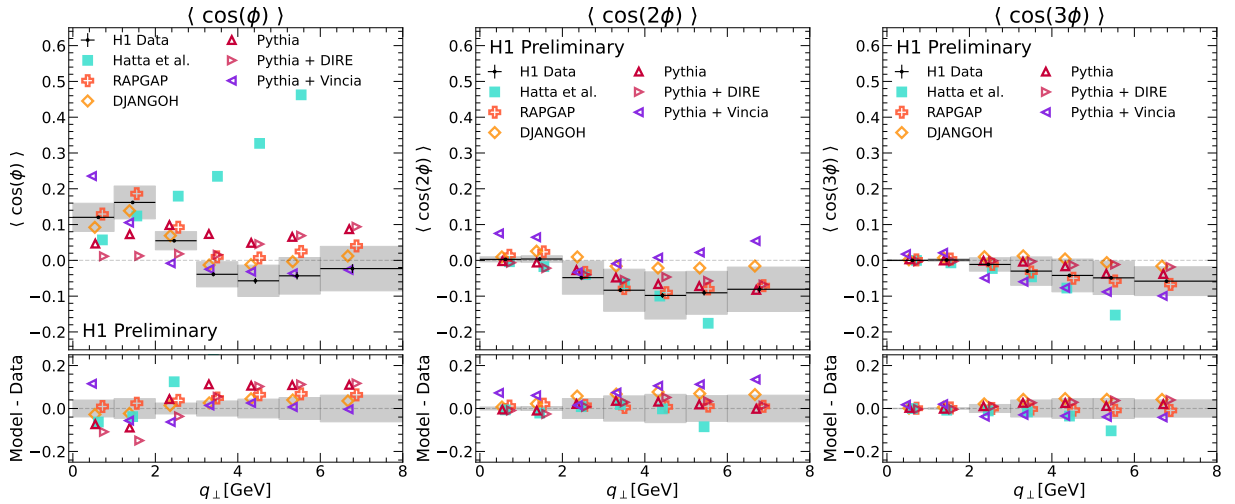
Fig. 3: Three harmonics of the azimuthal angular asymmetry between the lepton and leading jet as a function of $q_\perp$. Predictions from multiple simulations as well as a pQCD calculation are shown for comparison. The absolute difference between data and predictions is shown in the bottom panels.

7 Conclusions

A measurement of the azimuthal angular lepton-jet asymmetry in positron-proton collisions is presented. The measurement is shown as a function of the total transverse momentum, $q_\perp$. This observable is sensitive to initial and final state soft gluon radiation.

While theory predictions involving soft gluon resummation in the TMD factorization framework disagree with the measured data, there is reasonably good agreement between the measurement and DIS event generators DJANGOH and RAPGAP. Both the nominal PYTHIA results and alternative parton showers show large disagreements with data. This could indicate that non-perturbative contributions are larger than expected, or that the condition that $P_\perp \gg q_\perp$ begins to be compromised around $q_\perp \approx 3.0$ GeV. A measurement of the asymmetry angle using jets with a resolution parameter of R=0.4 would be a very logical follow up study. As the jet cone is smaller, less soft gluon radiaton would be reconstructed as part of the final state jet, and should result a larger measured asymmetry.

Results unfolded to generator level are reported using novel machine learning methods. All measured

quantities are calculated using previously unfolded results. The results presented in the work represent the first re-use of previous results of MULTIFOLD for a new observable. This is a key step towards demonstrating the potential for unfolding entire datasets with these novel machine learning methods, where collaborations can produce a multidude analyses from a single unfolding procedure.

Bibliography

[1] Yoshitaka Hatta, Bo-Wen Xiao, and Feng Yuan. Probing the Small- x Gluon Tomography in Correlated Hard Diffractive Dijet Production in Deep Inelastic Scattering. *Phys. Rev. Lett.*, 116(20):202301, 2016.

[2] Tolga Altinoluk, Néstor Armesto, Guillaume Beuf, and Amir H. Rezaeian. Diffractive Dijet Production in Deep Inelastic Scattering and Photon-Hadron Collisions in the Color Glass Condensate. *Phys. Lett. B*, 758:373–383, 2016.

[3] Jian Zhou. Elliptic gluon generalized transverse-momentum-dependent distribution inside a large nucleus. *Phys. Rev. D*, 94(11):114017, 2016.

[4] Yoshikazu Hagiwara, Yoshitaka Hatta, Roman Pasechnik, Marek Tasevsky, and Oleg Teryaev. Accessing the gluon Wigner distribution in ultraperipheral pA collisions. *Phys. Rev. D*, 96(3):034009, 2017.

[5] Heikki Mäntysaari, Niklas Mueller, and Björn Schenke. Diffractive Dijet Production and Wigner Distributions from the Color Glass Condensate. *Phys. Rev. D*, 99(7):074004, 2019.

[6] Heikki Mäntysaari, Niklas Mueller, Farid Salazar, and Björn Schenke. Multigluon Correlations and Evidence of Saturation from Dijet Measurements at an Electron-Ion Collider. *Phys. Rev. Lett.*, 124(11):112301, 2020.

[7] Daniel Boer, Stanley J. Brodsky, Piet J. Mulders, and Cristian Pisano. Direct Probes of Linearly Polarized Gluons inside Unpolarized Hadrons. *Phys. Rev. Lett.*, 106:132001, 2011.

[8] Andreas Metz and Jian Zhou. Distribution of linearly polarized gluons inside a large nucleus. *Phys. Rev. D*, 84:051503, 2011.

[9] Adrian Dumitru, Tuomas Lappi, and Vladimir Skokov. Distribution of Linearly Polarized Gluons and Elliptic Azimuthal Anisotropy in Deep Inelastic Scattering Dijet Production at High Energy. *Phys. Rev. Lett.*, 115(25):252301, 2015.

[10] Daniel Boer, Piet J. Mulders, Jian Zhou, and Ya-jin Zhou. Suppression of maximal linear gluon polarization in angular asymmetries. *JHEP*, 10:196, 2017.

[11] Daniël Boer, Piet J. Mulders, Cristian Pisano, and Jian Zhou. Asymmetries in Heavy Quark Pair and Dijet Production at an EIC. *JHEP*, 08:001, 2016.

[12] Hongxi Xing, Cheng Zhang, Jian Zhou, and Ya-Jin Zhou. The $\cos 2\phi$ azimuthal asymmetry in ρ^0 meson production in ultraperipheral heavy ion collisions. *JHEP*, 10:064, 2020.

[13] Ye-Yin Zhao, Ming-Mei Xu, Li-Zhu Chen, Dong-Hai Zhang, and Yuan-Fang Wu. Suppressions of dijet azimuthal correlations in the future EIC. *Phys. Rev. D*, 104(11):114032, 2021.

[14] Xuan-Bo Tong, Bo-Wen Xiao, and Yuan-Yuan Zhang. Harmonics of Parton Saturation in Lepton-Jet Correlations at the EIC. 11 2022.

[15] Yoshitaka Hatta, Bo-Wen Xiao, Feng Yuan, and Jian Zhou. Azimuthal angular asymmetry of soft gluon radiation in jet production. *Phys. Rev. D*, 104(5):054037, 2021.

[16] V. Andreev et al. Measurement of Lepton-Jet Correlation in Deep-Inelastic Scattering with the H1 Detector Using Machine Learning for Unfolding. *Phys. Rev. Lett.*, 128(13):132002, 2022.

[17] H1 Collaboration. Machine learning-assisted measurement of multi-differential lepton-jet correlations in deep-inelastic scattering with the H1 detector. *H1prelim-22-031*, 2022.

[18] Anders Andreassen, Patrick T. Komiske, Eric M. Metodiev, Benjamin Nachman, and Jesse Thaler. OmniFold: A Method to Simultaneously Unfold All Observables. *Phys. Rev. Lett.*, 124(18):182001, 2020.

[19] Anders Andreassen, Patrick T. Komiske, Eric M. Metodiev, Benjamin Nachman, Adi Suresh, and Jesse Thaler. Scaffolding Simulations witih Deep Learning for High-Dimensional Deconvolution. *ICLR SimDL Workshop*, page 12, 2021.

[20] H1 Collaboration. Multi-differential Jet Substructure Measurement in High Q^2 DIS Events with

HERA-II Data. *H1prelim-22-034*, 2022.

[21] Multidifferential study of identified charged hadron distributions in *Z*-tagged jets in proton-proton collisions at $\sqrt{s} =$ 13 TeV. 8 2022.

[22] I. Abt et al. The H1 detector at HERA. *DESY-93-103*, 7 1993.

[23] B. Andrieu et al. The H1 liquid argon calorimeter system. *Nucl. Instrum. Meth. A*, 336:460–498, 1993.

[24] I. Abt et al. The H1 detector at HERA. *Nucl. Instrum. Meth. A*, 386:310–347, 1997.

[25] I. Abt et al. The Tracking, calorimeter and muon detectors of the H1 experiment at HERA. *Nucl. Instrum. Meth. A*, 386:348–396, 1997.

[26] R. D. Appuhn et al. The H1 lead / scintillating fiber calorimeter. *Nucl. Instrum. Meth. A*, 386:397–408, 1997.

[27] D. Pitzl et al. The H1 silicon vertex detector. *Nucl. Instrum. Meth. A*, 454:334–349, 2000.

[28] B. Andrieu et al. Beam tests and calibration of the H1 liquid argon calorimeter with electrons. *Nucl. Instrum. Meth. A*, 350:57–72, 1994.

[29] B. Andrieu et al. Results from pion calibration runs for the H1 liquid argon calorimeter and comparisons with simulations. *Nucl. Instrum. Meth. A*, 336:499–509, 1993.

[30] F. D. Aaron et al. Determination of the Integrated Luminosity at HERA using Elastic QED Compton Events. *Eur. Phys. J. C*, 72:2163, 2012. [Erratum: Eur.Phys.J.C 74, 2733 (2014)].

[31] C. Adloff et al. Measurement and QCD analysis of neutral and charged current cross-sections at HERA. *Eur. Phys. J. C*, 30:1–32, 2003.

[32] F. D. Aaron et al. Inclusive Deep Inelastic Scattering at High Q^2 with Longitudinally Polarised Lepton Beams at HERA. *JHEP*, 09:061, 2012.

[33] V. Andreev et al. Measurement of multijet production in *ep* collisions at high Q^2 and determination of the strong coupling α_s. *Eur. Phys. J. C*, 75(2):65, 2015.

[34] V. Andreev et al. Measurement of Jet Production Cross Sections in Deep-inelastic *ep* Scattering at HERA. *Eur. Phys. J. C*, 77(4):215, 2017. [Erratum: Eur.Phys.J.C 81, 739 (2021)].

[35] Ursula Bassler and Gregorio Bernardi. On the kinematic reconstruction of deep inelastic scattering at HERA: The Sigma method. *Nucl. Instrum. Meth. A*, 361:197–208, 1995.

[36] Matteo Cacciari, Gavin P. Salam, and Gregory Soyez. FastJet User Manual. *Eur. Phys. J. C*, 72:1896, 2012.

[37] Matteo Cacciari and Gavin P. Salam. Dispelling the N^3 myth for the k_t jet-finder. *Phys. Lett. B*, 641:57–61, 2006.

[38] S. Catani, Yuri L. Dokshitzer, M. H. Seymour, and B. R. Webber. Longitudinally invariant K_t clustering algorithms for hadron hadron collisions. *Nucl. Phys. B*, 406:187–224, 1993.

[39] Stephen D. Ellis and Davison E. Soper. Successive combination jet algorithm for hadron collisions. *Phys. Rev. D*, 48:3160–3166, 1993.

[40] M Peez. Search for deviations from the standard model in high transverse energy processes at the electron proton collider HERA. (Thesis, Univ. Lyon), 2003.

[41] S Hellwig. Untersuchung der D^* - π slow Double Tagging Methode in Charmanalysen. (Diploma, Univ. Hamburg), 2005.

[42] B Portheault. First measurement of charged and neutral current cross sections with the polarized positron beam at HERA II and QCD-electroweak analyses. (Thesis, Univ. Paris XI), 2005.

[43] K. Charchula, G. A. Schuler, and H. Spiesberger. Combined QED and QCD radiative effects in deep inelastic lepton - proton scattering: The Monte Carlo generator DJANGO6. *Comput. Phys. Commun.*, 81:381–402, 1994.

[44] Hannes Jung. Hard diffractive scattering in high-energy e p collisions and the Monte Carlo gener-

ator RAPGAP. *Comput. Phys. Commun.*, 86:147–161, 1995.

[45] H Spiesberger, A A Akhundov, H Anlauf, Dimitri Yuri Bardin, Johannes Blümlein, H D Dahmen, Stanislaw Jadach, L V Kalinovskaya, A Kwiatkowski, P Manakos, T Mannel, H J Möhring, G Montagna, O Nicrosini, T Ohl, Wiesiek Placzek, Tord Riemann, and L Viola. Radiative corrections at HERA. *CERN-TH-6447-92*, page 43, Mar 1992.

[46] A Kwiatkowski, H. Spiesberger, and H. J. Mohring. Characteristics of radiative events in deep inelastic e p scattering at HERA. *Z. Phys. C*, 50:165–178, 1991.

[47] A. Kwiatkowski, H. Spiesberger, and H. J. Mohring. Heracles: An Event Generator for *ep* Interactions at HERA Energies Including Radiative Processes: Version 1.0. *Comput. Phys. Commun.*, 69:155–172, 1992.

[48] J. Pumplin, D. R. Stump, J. Huston, H. L. Lai, Pavel M. Nadolsky, and W. K. Tung. New generation of parton distributions with uncertainties from global QCD analysis. *JHEP*, 07:012, 2002.

[49] B. Andersson, G. Gustafson, G. Ingelman, and T. Sjöstrand. Parton fragmentation and string dynamics. *Phys. Rept.*, 97:31–145, 1983.

[50] S. Schael et al. Bose-Einstein correlations in W-pair decays with an event-mixing technique. *Phys. Lett. B*, 606:265–275, 2005.

[51] L. Lönnblad. ARIADNE version 4: A Program for simulation of QCD cascades implementing the color dipole model. *Comput. Phys. Commun.*, 71:15–31, 1992.

[52] R. Brun, F. Bruyant, M. Maire, A. C. McPherson, and P. Zanarini. GEANT3. *CERN-DD-EE-84-01*, 9 1987.

[53] Torbjorn Sjöstrand, Stephen Mrenna, and Peter Z. Skands. PYTHIA 6.4 physics and manual. *JHEP*, 05:026, 2006.

[54] Torbjörn Sjöstrand, Stefan Ask, Jesper R. Christiansen, Richard Corke, Nishita Desai, Philip Ilten, Stephen Mrenna, Stefan Prestel, Christine O. Rasmussen, and Peter Z. Skands. An introduction to PYTHIA 8.2. *Comput. Phys. Commun.*, 191:159–177, 2015.

[55] Walter T. Giele, David A. Kosower, and Peter Z. Skands. A simple shower and matching algorithm. *Phys. Rev. D*, 78:014026, 2008.

[56] Walter T. Giele, Lisa Hartgring, David A. Kosower, Eric Laenen, Andrew J. Larkoski, Juan J. Lopez-Villarejo, Mathias Ritzmann, and Peter Skands. The Vincia Parton Shower. *PoS*, DIS2013:165, 2013.

[57] Stefan Höche and Stefan Prestel. The midpoint between dipole and parton showers. *Eur. Phys. J. C*, 75(9):461, 2015.

[58] Richard D. Ball et al. Parton distributions from high-precision collider data. *Eur. Phys. J. C*, 77(10):663, 2017.

[59] L. A. Harland-Lang, A. D. Martin, P. Motylinski, and R. S. Thorne. Parton distributions in the LHC era: MMHT 2014 PDFs. *Eur. Phys. J. C*, 75(5):204, 2015.

[60] Johannes Bellm et al. Herwig 7.0/Herwig++ 3.0 release note. *Eur. Phys. J. C*, 76(4):196, 2016.

[61] M. Bahr et al. Herwig++ Physics and Manual. *Eur. Phys. J. C*, 58:639–707, 2008.

[62] Sayipjamal Dulat, Tie-Jiun Hou, Jun Gao, Marco Guzzi, Joey Huston, Pavel Nadolsky, Jon Pumplin, Carl Schmidt, Daniel Stump, and C. P. Yuan. New parton distribution functions from a global analysis of quantum chromodynamics. *Phys. Rev. D*, 93(3):033006, 2016.

[63] V. Andreev, M. Arratia, Baghdasaryan, et al. Measurement of lepton-jet correlation in deep-inelastic scattering with the h1 detector using machine learning for unfolding. *Phys. Rev. Lett.*, 128:132002, Mar 2022.

[64] Trevor Hastie, Robert Tibshirani, and Jerome Friedman. *The Elements of Statistical Learning*. Springer Series in Statistics. Springer New York Inc., New York, NY, USA, 2001.

[65] Masashi Sugiyama, Taiji Suzuki, and Takafumi Kanamori. *Density Ratio Estimation in Machine*

Learning. Cambridge University Press, 2012.

[66] Martín Abadi, Paul Barham, Jianmin Chen, Zhifeng Chen, Andy Davis, Jeffrey Dean, Matthieu Devin, Sanjay Ghemawat, Geoffrey Irving, Michael Isard, et al. Tensorflow: A system for large-scale machine learning. *OSDI*, 16:265, 2016.

[67] Fraciois Chollet. Keras. https://github.com/fchollet/keras, 2017.

[68] Diederik Kingma and Jimmy Ba. Adam: A method for stochastic optimization. *ICLR*, 3, 2015.

[69] Xavier Glorot and Yoshua Bengio. Understanding the difficulty of training deep feedforward neural networks. In Yee Whye Teh and D. Mike Titterington, editors, *AISTATS*, volume 9 of *JMLR Proceedings*, pages 249–256. JMLR.org, 2010.

[70] Roman Kogler. Measurement of jet production in deep-inelastic ep scattering at hera, Feb 2011.

[71] V. Andreev et al. Measurement of multijet production in ep collisions at high Q^2 and determination of the strong coupling α_s. *Eur. Phys. J. C*, 75(2):65, 2015.

[72] F. D. Aaron et al. Measurement of $D^{*\pm}$ Meson Production and Determination of $F_2^{c\bar{c}}$ at low Q^2 in Deep-Inelastic Scattering at HERA. *Eur. Phys. J. C*, 71:1769, 2011. [Erratum: Eur.Phys.J.C 72, 2252 (2012)].

[73] F. D. Aaron et al. Inclusive Deep Inelastic Scattering at High Q^2 with Longitudinally Polarised Lepton Beams at HERA. *JHEP*, 09:061, 2012.

[74] B. Efron. Bootstrap Methods: Another Look at the Jackknife. *The Annals of Statistics*, 7(1):1 – 26, 1979.

[75] Jeffrey Berger and Anna Stasto. Numerical solution of the nonlinear evolution equation at small x with impact parameter and beyond the LL approximation. *Phys. Rev. D*, 83:034015, 2011.

[76] Javier L. Albacete, Nestor Armesto, Jose Guilherme Milhano, Paloma Quiroga-Arias, and Carlos A. Salgado. AAMQS: A non-linear QCD analysis of new HERA data at small-x including heavy quarks. *Eur. Phys. J. C*, 71:1705, 2011.

[77] Tie-Jiun Hou et al. New CTEQ global analysis of quantum chromodynamics with high-precision data from the LHC. *Phys. Rev. D*, 103(1):014013, 2021.

Appendices